

The D^2 Variation for Isolated LOX Drops and Polydisperse Clusters in Hydrogen at High Temperature and Pressures

K. HARSTAD and J. BELLAN*

Jet Propulsion Laboratory, California Institute of Technology, 4800 Oak Grove Drive, MS 125-109,
Pasadena, CA 91109-8099, USA

A study of the d^2 variation for isolated fluid drops and for fluid drops belonging to polydisperse clusters has been conducted at a high temperature and elevated pressures. The mathematical formulation is based on a previously validated model of subcritical/supercritical isolated fluid drop behavior. Coupled with the isolated drop equations, a set of conservation equations has been developed to describe the global cluster behavior. All these equations are based on the general transport matrix including Soret and Dufour terms and they are consistent with nonequilibrium thermodynamics and at low pressure with kinetic theory. Moreover, the model also accounts for real gas effects through accurate equations of state and for correct values of the transport properties in the high pressure, high temperature regime. The model has been first exercised for isolated LOX drops in H_2 at pressures ranging from 1.5 MPa (subcritical pressure for O_2) to 20 MPa (supercritical pressure for O_2). The results show that while at subcritical pressures the d^2 variation is nearly linear, with increasing pressure it departs considerably from the linear behavior; the largest departure occurs in the vicinity of the oxygen critical point. The slope of $d^2(t)$ was fitted using both a constant and a linear fit, and it was shown that the linear fit provides a better alternative for correlation purposes. Simulations were also conducted for clusters of LOX drops in H_2 in the range 6 to 40 MPa (reduced pressures of 1.2–8 with respect to pure O_2). Parametric studies of the effect of the thermal diffusion factor value reveal that it is minor at 10 MPa and moderate at 40 MPa, and that although the Soret term is dominated by the Fick, Dufour, and Fourier terms, it is not negligible. The influence of a cluster Nusselt number is also shown to be relatively small in the range 10^3 to 10^4 , consistent with the supercritical behavior being essentially a diffusive one. All of the results show a nonlinear d^2 variation with curves having a positive curvature independent of the values of the thermal diffusion factor, the Nusselt number or the LOX/ H_2 mass ratio. The approximation of a binary size cluster containing relatively a much larger number of small drops by a monodisperse cluster with a drop size based upon the surface average of the drops in the polydisperse cluster yields a good evaluation of the thermodynamic quantities in the interstitial drop region but an underestimate of the lifetime of the drops in the cluster. © 2001 by The Combustion Institute

NOMENCLATURE

A	area
A_J	coefficient in the transport matrix
A_q	coefficient in the transport matrix
B_J	coefficient in the transport matrix
B_q	coefficient in the transport matrix
C_p	heat capacity at constant pressure
C_q	coefficient in the transport matrix
D	mass diffusion coefficient
e	energy
h	molar enthalpy
\bar{J}	molar flux
Le	Lewis number
m	molar mass
M	mass
n	molar density

N	number of drops
Nu	Nusselt number
p	pressure
\dot{q}	heat flux
r	radial coordinate
R	specific radial position
R_u	universal gas constant
S	surface
t	time
T	temperature
u	radial velocity
v	molar volume
V	volume
X	molar fraction
Y	mass fraction
Z	compression factor

Greek Symbols

α_{BK}	Bearman–Kirkwood thermal diffusion factor
---------------	---

*Corresponding author: J. Bellan, California Inst. of Technology 4800 Oak Grove Dr., MS 125-109, Pasadena, CA 91109. E-mail: josette.bellan@jpl.nasa.gov

α_D	mass diffusion factor
α_h	defined by Eq. 13
α_{IK}	Irwing-Kirkwood thermal diffusion factor
α_v	thermal expansion ratio
γ	activity coefficient
η	viscosity
κ	isentropic compressibility
λ	thermal conductivity
ρ	density
τ	stress tensor
ϕ	LOX/H_2 mass ratio
Φ_v	viscous dissipation
φ	fugacity coefficient

Subscripts

c	critical
C	cluster
d	drop
e	external
j	species
r	reduced value; radial direction
s	'optical' boundary
α	drop size class
1	O_2 or LOX

Superscripts

0	initial condition
i	interstitial
si	sphere of influence

INTRODUCTION

The interest in controlling fluid disintegration, mixing, and combustion in liquid rocket chambers has led to investigations of liquid oxygen (LOX) at high pressures, p , and sometimes also at high temperatures, T . A literature review including high (p , T) drop studies appeared in Givler and Abraham [1], and more recently Bellan [2] surveyed investigations of drops, streams, shear and mixing layers, jets and sprays. Among these studies, most noteworthy experimental investigations of LOX are those of Chesnau et al. [3] for single drops, and those of Krülle and Mayer [4], Mayer and Tamura [5], Mayer et al. [6, 7], Chehroudi et al. [8, 9], Ivancic et al. [11], and Oschwald et al. [10] exploring fluid jet breakup at supercritical pres-

ures such as encountered in liquid rocket combustors. These recent observations of fluid jet breakup at supercritical pressures have identified a fluid disintegration mechanism that is very different from classical atomization. It was reported that there is a noticeable difference in the outcome of fluid disintegration according to the surrounding pressure: whereas in the subcritical regime ligaments and drops were easily observed, in the transcritical regime atomization was inhibited. Furthermore, in the supercritical regime, the ligaments identified at subcritical pressures were replaced by thin threads of fluid extruding from the jet in the near field, followed by big chunks of irregularly shaped fluid in the far field. Simple calculations by Snyder et al. [12] showed that these big chunks of irregularly shaped fluid are organized in dense clusters, as the estimated ratio of the separation distance to the average equivalent-drop radius (in the estimate, for simplicity, the spray was assumed to consist of drops) was approximately 3 to 6. Because previous studies of drop clusters at subcritical pressures have revealed the role of polydispersity for liquid drops [13], the question arises if the same conclusions apply to fluid chunks or drops at supercritical pressures. Because the evaporation of drops at subcritical conditions is governed by a convective-diffusive process (the governing convection arises from evaporation), whereas supercritical drop behavior is governed by a diffusive process [14, 15], the inference from one situation to the other may not hold.

Early models of single, isolated drops at high pressures have been developed by Rosner [16, 17] and by Umemura [18]. More recent models have been formulated by Jia and Gogos [19, 20], Delplanque and Sirignano [21], Yang and collaborators [22, 23], Daou et al. [24], Umemura and Shimada [25, 26], and Harstad and Bellan [14, 15, 27, 28]. Given the variation in the modeling of the equations of state, the fluid properties at high pressure and of the definition of the drop boundary (which in all studies except [14, 15, 27, 28] is assumed to be a material surface), and considering the differences among the predictions of the different investigations, the only way to gain confidence in a model's predictive capabilities is through validation with data. Such validation was con-

ducted by Harstad and Bellan [14, 15] using the microgravity heptane/nitrogen data of Nomura et al. [29] in absence of combustion; a small part of the data was used to determine the value of the thermal diffusion factor (the transport coefficient introduced by the Soret and Dufour terms; see below), and the remaining part of the data was used to validate the model using the determined thermal diffusion factor. The comparisons covered the entire range of pressures and temperatures of the data, and given the difference between the configuration of the experiments that were conducted with suspended drops and that of the simulations that were of free floating drops, the agreement was good. The comparison was made between the timewise evolution of the observed diameter squared, d^2 , and that computed, as well as between the experimental versus the calculated maximum slope of these curves. The agreement was on average within 15% for the slopes of the curves, whereas the agreement between the d^2 profiles was excellent in the low p regime, with deviations occurring with increased p . These deviations are consistent with the estimates of Morin [30] who showed that the suspending fiber has an increasing influence on the drop heat up with increasing T and p .

The goal of this study is to investigate the timewise evolution of d^2 both for single, isolated drops and for drops in polydisperse clusters, at high pressure conditions. The isolated drop study covers subcritical to supercritical pressures (with respect to critical pressure of O_2) range and identifies the fluid-drop interaction. Simulations with clusters of drops are conducted only at supercritical pressures so as to emulate the general environment of a liquid rocket combustion chamber. Throughout this paper, the supercritical regime is defined as that above either one of the critical pressure or temperature so as to coincide with the thermodynamic region where a two phase region does not exist. Furthermore, since the critical values depend not only upon pressure and temperature, but also upon composition, supercriticality is here arbitrarily defined with respect to the O_2 critical properties.

The interest in predicting the d^2 variation stems not only from the fact that d^2 is generally the sole information provided from experi-

ments, and therefore, the only quantity that can be compared, but it is also used in practical, rocket combustion codes where it is assumed to have the linear time decay typical of subcritical behavior (the d^2 -law). The question that arises then is if d^2 indeed varies linearly with time for *LOX* drops in hydrogen at high pressure conditions. This question will be answered below both for isolated drops and for drops belonging to polydisperse clusters. The study on polydispersity effects is conducted by taking as an example a cluster having a binary size distribution. Although studies of high pressure drop interactions exist (Jiang and Chiang [31–33], and Harstad and Bellan [34]), they are currently limited to monodisperse clusters of drops and it is uncertain if polydispersity effects are important at high pressures. Below we briefly explain a model of supercritical-fluid individual-drop behavior that has been documented in detail elsewhere [14, 15], recall the single drop conservation equations and only highlight specific aspects of the boundary conditions. Then, we present the drop cluster equations for a polydisperse cluster, extending our previous monodisperse study [34]. When analyzing the results, we first focus on isolated drops and then discuss the effect of polydispersity. For polydisperse clusters, we begin by discussing results directed at understanding the effect of two parameters whose value is relatively uncertain, namely that of the thermal diffusion factor for the $O_2 - H_2$ system and of the effective cluster Nusselt number. Further, we investigate the effects of the far field pressure and that of the drop to surrounding fluid mass ratio, and finally explore the merit of the monodisperse approximation.

MODEL

The fluid drop model is based upon Keizer's fluctuation-dissipation (FD) theory [35], which has the distinct advantage of formally accounting for nonequilibrium processes as well as naturally relating fluxes and forces for a general fluid by providing the form of the flux matrix, a form that continuum theory does not provide. Indeed, it is customary within the continuum formulation to extend, without a firm justification, the kinetic theory of rarified gases to

describe the fluxes for more general cases. The viewpoint of fluctuation-dissipation theory is intermediate to that of continuum and molecular-level approaches and allows the modeling of transport processes totally consistent with non-equilibrium thermodynamics [36]. Furthermore, although of only academic relevance herein, in the low pressure limit the FD theory is consistent with kinetic theory [37]. The main result of the FD theory is the form of the transport matrix which now includes two terms for each of the molar and heat fluxes; the molar flux is the sum of Fickian terms and the Soret term, whereas the heat flux term is the sum of the Fourier term and the Dufour term. A detailed description of the model can be found in [27] and [15], and will not be repeated here. This model has been exercised with accurate equations of state [38], accurate transport properties [27], and appropriate boundary conditions [14, 15, 27] without any assumption regarding phase equilibrium or existence of a drop material surface. Validation of the single drop model for a binary mixture [14, 15] included the finding of the only unknown transport coefficient, the thermal diffusion factor, from comparison with part of the data. Here the model is exercised in the context of O_2/H_2 with values of the thermal diffusion factor inferred from the list in [37], and a sensitivity study is conducted in the context of fluid drop clusters.

Single Drop Conservation Equations

The single drop conservation equations are simply recalled, and the reader is referred for the detailed derivation to [15]. These conservation equations, in spherical geometry, pertain to the entire field, $0 \leq r \leq R^{si}$, not only to the drop. Here r is the radial coordinate and R^{si} is the location of the far field boundary which must be specified for single drop calculations. The conservation equations are:

-Continuity

$$\frac{\partial \rho}{\partial t} + \frac{1}{r^2} \frac{\partial(r^2 \rho u)}{\partial r} = 0 \quad (1)$$

where ρ is the mass density, u is the radial velocity, and t is the time.

-Momentum conservation

$$\frac{\partial(\rho u)}{\partial t} + \frac{1}{r^2} \frac{\partial(r^2 \rho u u)}{\partial r} + \frac{\partial p}{\partial r} = \frac{\partial \tau_{rr}}{\partial r} + \frac{3 \tau_{rr}}{r} \quad (2)$$

where $\tau_{rr} = (4/3)\eta[\partial u/\partial r - u/r]$ is the stress tensor and η is the mixture viscosity.

-Species conservation

$$\rho \frac{DY_j}{Dt} = -m_j \nabla \cdot \vec{J}_j \quad (3)$$

where Y_j is the mass fraction of species j , \vec{J}_j is the molar flux, m_j is the molar mass of species j , and $D/Dt \equiv \partial/\partial t + u(\partial/\partial r)$.

-Energy equation

$$nC_p \frac{DT}{Dt} = \alpha_v T \frac{Dp}{Dt} - \nabla \cdot \vec{q} + \Phi_v + \sum_j^N h_j \nabla \cdot \vec{J}_j \quad (4)$$

where n is the molar density, \vec{q} is the heat flux, C_p is the mixture molar heat capacity at constant pressure, $h_j = (\partial h/\partial X_j)_{p, X_{i \neq j}}$ is the partial molar enthalpy of species j where X_j is the molar fraction of species j , $\alpha_v = [(\partial v/\partial T)_{p, X_j}]/v$ is the thermal expansion ratio with v being the molar volume, and $\Phi_v = (4/3)\eta[\partial u/\partial r - u/r]^2$ is the viscous dissipation. For a binary mixture (subscripts 1 and 2) the radial fluxes are

$$-J_{1r} = A_J \frac{\partial Y_1}{\partial r} + B_J \frac{\partial T}{\partial r} + C_J \frac{\partial p}{\partial r} \quad (5)$$

$$-q_r = A_q \frac{\partial T}{\partial r} + C_q \frac{\partial Y_1}{\partial r} + B_q \frac{\partial p}{\partial r}$$

with the coefficients

$$A_J = (m/m_1)nD\alpha_D \quad (6)$$

$$B_J = (m_2/m)nDX_1X_2(\alpha_{IK} - \alpha_h)/T \quad (7)$$

$$C_J = (m_2/m)nD(m_1m_2X_1X_2/m) \cdot (v_1/m_1 - v_2/m_2)/(R_u T) \quad (8)$$

$$A_q = \lambda + (\alpha_{IK} - \alpha_h)\alpha_{IK}R_u nDX_1X_2 \quad (9)$$

$$C_q = [m^2/(m_1m_2)]nD\alpha_D\alpha_{IK}R_u T \quad (10)$$

$$B_q = nD\alpha_{IK}(m_1m_2X_1X_2/m)(v_1/m_1 - v_2/m_2) \quad (11)$$

where $m = X_1m_1 + X_2m_2$ is the mixture molar mass, v_j is the partial molar volume, R_u is the

universal gas constant, λ is the thermal conductivity, α_{IK} is the Irving–Kirkwood thermal diffusion factor [39], and D is the mixture diffusivity.

According to the Gibbs–Duhem relationship, the mass diffusion factor, $\alpha_D = \alpha_{D11} = \alpha_{D22} = -\alpha_{D12} = -\alpha_{D21}$ and from thermodynamics

$$\alpha_D = 1 + X_1 \partial \ln \gamma_1 / \partial X_1 \quad (12)$$

where $\gamma_1 \equiv \varphi_1 / \varphi_1^o$ is the activity coefficient and φ is the fugacity coefficient with the superscript o denoting the pure ($X_1 = 1$) limit. It was shown by Harstad and Bellan [14, 15] that the Bearman–Kirkwood thermal diffusion factor, α_{BK} , and α_{IK} , derived from connected forms of the heat flux [39], are related by

$$\alpha_{BK} = \alpha_{IK} - \alpha_h, \quad \alpha_h \equiv (m_1 m_2 / m) \cdot (h_1 / m_1 - h_2 / m_2) / (R_u T). \quad (13)$$

In the above derivation (c.f. Eq. 6), it has been carefully ensured that the expression for the thermal conductivity converges to the kinetic value in the low pressure limit [14, 15], and thus its value is indeed that tabulated or calculated through corresponding states procedures [40].

To close the system of equations, equations of state (EOSs) were coupled to the above system of differential equations. The EOSs used in conjunction with the conservation statements were the real gas EOSs derived in [38].

The boundary conditions were discussed in detail in Harstad and Bellan [14, 15], and the reader is referred to those publications for details. We distinguish between the Lagrangian location of the initial drop boundary, R_d^0 , which is followed in time, $R_d(t)$, and the location of the ‘optical’ drop boundary, $R_s(t)$, which is also followed in time. The important concept to be retained is that we do not assume the existence of a material interface in the region $0 \leq r \leq R^{si}$. If such an interface exists at any time, it is totally consistent with our definition whereby the drop boundary (not necessarily an interface) is identified to be at the location of the largest density gradient, $r = R_s$; this is relevant to optical observations which identify changes in the index of refraction. Furthermore, no assumption is made regarding phase equilibrium at that boundary, or anywhere else in the computational domain.

The numerical method was also explained in detail elsewhere [15], and thus will not be repeated.

Conservation Equations for a Polydisperse Cluster

The configuration is that of a spherical cluster of volume V_C , boundary area A_C and radius R_C containing N spherical LOX fluid drops immersed in quiescent H_2 with far field surroundings denoted by the subscript “e”. The N drops are partitioned into K size classes denoted by α and there are N_α drops in each size class with $N = \sum_{\alpha=1}^K N_\alpha$. We assume that the interstitial region between drops is uniform and quiescent with respect to the cluster, the implication being that we address only average properties of the fluid in the interstitial region. With these definitions, we generalize the monodisperse formulation presented in Harstad and Bellan [34] to the situation of a polydisperse cluster of fluid drops. As in [34], we define a ‘sphere of influence’ around each drop that is centered at the drop center and has a radius, R^{si} (superscript “si” refers here to the sphere of influence). The value of R^{si} is one half of the mean distance between adjacent drops, or less, and is found from the condition that the spheres of influence must be tightly packed (in contrast with the isolated drop simulations where $R^{si,0}$ is specified, here it is calculated). The Lagrangian value of R^{si} for each size class is R_α and its corresponding volume, V_α , which contains the drop and its surrounding fluid has by definition a fixed mass; this means that the V_α boundary is a function of time to accommodate the change in density due to heating. The volume of the interstitial region of the cluster is $V^i = V_C - \sum_{\alpha=1}^K N_\alpha V_\alpha$ and it is in this volume that the conservation equations are stated below in a Lagrangian frame; the superscript i refers to the values in the interstitial region. These are conservation of mass, species j , and energy $e^i = h^i / m^i - p^i / \rho^i$:

$$\begin{aligned} d\rho^i/dt &= 0, \quad d\rho_j^i/dt = -m_j \nabla \cdot \vec{J}_j^i, \\ d(p^i e^i)/dt &= -\nabla \cdot \vec{q}^i \end{aligned} \quad (14)$$

all in V^i . Integrating the conservation equations in V^i yields

$$\begin{aligned}\frac{d}{dt} \left(\int_{V^i} \rho^i dV^i \right) &= 0, \\ \frac{d}{dt} \left(\int_{V^i} \rho_j^i dV^i \right) &= - \int_{S^i} m_j \vec{J}_j^i \cdot d\vec{A}, \\ \frac{d}{dt} \left[\int_{V^i} (\rho^i/h^i/m^i - p^i) dV^i \right] &= - \int_{S^i} \vec{q}^i \cdot d\vec{A} \quad (15)\end{aligned}$$

where A is the area of V^i 's boundary, S^i , and we account for the null relative velocity with respect to S^i . The first equation of Eqs. 15 has a simple integral $V^i(t) = M^i/\rho^i$ where M^i is the constant mass in V^i . The species and heat contributions to V^i arise both from the interaction of the cluster with its surroundings through fluxes of species and heat across the cluster's external boundary and from the interaction of V^i with all drops. Thus, the second and third equations in Eq. 15 become

$$\begin{aligned}\frac{dY_j^i}{dt} &= \frac{m_j}{M^i} \left(J_{je} A_C - \sum_{\alpha=1}^{\alpha=K} N_{\alpha} J_{j,\alpha} A_{\alpha} \right), \\ \frac{d}{dt} (h^i/m^i - p_e/\rho^i) &= \frac{1}{M^i} \left(q_e A_C - \sum_{\alpha=1}^{\alpha=K} N_{\alpha} q_{\alpha} A_{\alpha} \right) \quad (16)\end{aligned}$$

where Y_j^i is the interstitial mass fraction of species j and A_{α} is the boundary of V_{α} . The second equation in Eq. 16 can be transformed through thermodynamic relationships for a binary mixture into an equation for the interstitial temperature T^i

$$\begin{aligned}\tilde{C}_V \frac{dT^i}{dt} &= \frac{1}{M^i} \left[(q_e - m_1 \tilde{h} J_{1e}) A_C \right. \\ &\quad \left. - \sum_{\alpha=1}^{\alpha=K} N_{\alpha} (q_{\alpha} - m_1 \tilde{h} J_{1,\alpha}) A_{\alpha} \right] \\ &\quad - \tilde{\kappa}_s \frac{p_e}{\rho^i} \frac{dp_e}{dt} \quad (17)\end{aligned}$$

with

$$\begin{aligned}\tilde{C}_V &\equiv C_p^i/m^i - \alpha_v^i p_e/\rho^i, \\ \tilde{\kappa}_s &\equiv \kappa_s^i - \tilde{C}_V m^i \alpha_v^i T^i / (p_e C_p^i), \\ \tilde{h} &\equiv (h_1^i/m_1 - h_2^i/m_2) - p_e (v_1^i/m_1 - v_2^i/m_2),\end{aligned}$$

where C_p^i , α_v^i , κ_s^i , h_j^i , and v_j^i are the molar heat capacity, the thermal expansion ratio, the isentropic compressibility, the partial molar enthalpy and the partial molar volume of species j , all in V^i . The values of $J_{1,\alpha}$ and q_{α} are calculated at the edge of the sphere of influence for each size class according to the model of [27]. Fluxes J_{1e} and q_e are calculated according to a formalism introduced in [27] as

$$\begin{aligned}J_{1e} &= A_j^i (\partial Y_1 / \partial r)_{r=e} + B_j^i (\partial T / \partial r)_{r=e}, \\ q_e &= A_q^i (\partial T / \partial r)_{r=e} + C_q^i (\partial Y_1 / \partial r)_{r=e} \quad (18)\end{aligned}$$

where $j = 1$ refers to *LOX*, r is the direction normal to the cluster boundary enclosing V_C and paralleling the isolated drop model

$$\begin{aligned}A_j^i &= (\rho^i/m_1) D^i \alpha_D^i, \\ B_j^i &= (m_2/m^i) n^i D^i X_1^i X_2^i \alpha_{BK}^i T^i \quad (19)\end{aligned}$$

$$\begin{aligned}A_q^i &= \lambda^i + \alpha_{BK}^i \alpha_{IK}^i R_u n^i D^i X_1^i X_2^i, \\ C_q^i &= [m^i \rho^i / (m_1 m_2)] D^i \alpha_D^i \alpha_{IK}^i R_u T^i \quad (20)\end{aligned}$$

where n^i , D^i , λ^i , X_j^i , and α_D^i are calculated in V^i . The pressure gradient terms have been neglected in Eq. 18 since the Mach number being $\ll 1$, they have been found negligible. Similarly to the isolated drop model, the two forms of the thermal diffusion factor are

$$\begin{aligned}\alpha_{BK}^i &= \alpha_{IK}^i - \alpha_h^i, \\ \alpha_h^i &\equiv (m_1 m_2 / m^i) (h_1^i / m_1 - h_2^i / m_2) / (R_u T^i). \quad (21)\end{aligned}$$

Also,

$$\alpha_D^i = \alpha_{D11}^i = 1 + X_1^i \partial \ln \gamma_1^i / \partial X_1^i. \quad (22)$$

At the boundary of the spherical cluster we approximate the gradients by a difference across an external length scale r_e

$$\begin{aligned}(\partial Y_1 / \partial r)_{r=e} &= (Y_{1e} - Y_1^i) / r_e, \\ (\partial T / \partial r)_{r=e} &= (T_e - T^i) / r_e \quad (23)\end{aligned}$$

which may be related to what is equivalent to a Nusselt number, Nu_C , through $r_e = R_C/Nu_C$ because it is the characteristic distance over which transport occurs at the cluster boundary. Here, Nu_C is a parameter whose value is prescribed and whose influence will be studied.

Replacing Eqs. 19 and 20 into Eq. 18 yields

$$(q_e - m_1 \tilde{h} J_{1e}) A_C = [3V_C/(4\pi)]^{1/3} 4\pi Nu_C \cdot [(A_q^i - m_1 \tilde{h} B_J^i)(T_e - T^i) + (C_q^i - m_1 \tilde{h} A_J^i)(Y_{1e} - Y_1^i)] \quad (24)$$

$$J_{1e} A_C = [3V_C/(4\pi)]^{1/3} 4\pi Nu_C [A_J^i(Y_{1e} - Y_1^i) + B_J^i(T_e - T^i)] \quad (25)$$

which provides the necessary information for Eqs. 16 and 17.

The drop model for each size class used in conjunction with the interstitial equations is the same as that for single drops, as is the numerical method.

The system of equations for the interstitial region is closed by the addition of the real gas EOSs derived in [38], with unknowns T^i and Y_1^i since ρ^i is determined by the EOS. Once ρ^i is known, V^i and V_C are calculated. During each time step, the total differential Eqs. 16 and 17 are solved using a second order predictor-corrector method as described in [27].

RESULTS

Isolated-drop simulations were performed for both subcritical and supercritical pressures (for O_2 : $T_c = 154.6$ K, $p_c = 5.043$ MPa; for H_2 : $T_c = 33.2$ K, $p_c = 1.313$ MPa); however, drop cluster simulations were conducted only for pressures above p_c for O_2 so as to simulate a range of conditions pertinent to liquid rocket combustion chambers. The viscosity and thermal conductivity were calculated using conventional mixing rules where the individual species properties were calculated as in [27]. The mass diffusivity calculation over a large range of pressures and temperatures is also described in [27]; with this model, the diffusivity values converge to the respective liquid and gas ones in the proper limits. An O_2/H_2 thermal diffusion fac-

tor value is listed in [37] at one temperature, and adopted here as the baseline; to understand the impact of the chosen value, a sensitivity study is conducted in the context of drop clusters. The value listed [37] being that of α_{BK} (since it is α_{BK} that converges at low pressure to the kinetic theory limit), it is this parameter which is here varied over the listed range.

Isolated Drops

In all single drop calculations $\alpha_{BK} = 0.2$. All simulations were performed for an initial drop radius $R_d^0 = 5 \times 10^{-3}$ cm and $T_d^0 = 120$ K. The far field conditions are located at $R^{si,0} = 0.1$ cm where there is only pure H_2 and the temperature is 1000 K. Several simulations were conducted for pressures of 1.5, 3, 6, 10, and 20 MPa (reduced pressure of 0.3, 0.6, 1.2, 2, and 4 with respect to the p_c of O_2). To avoid an initial unphysical discontinuity, a minute amount of O_2 exists initially in the drop surroundings, its distribution vanishing with increasing r . Therefore, although the fluid drop temperature and outer fluid composition are assumed initially nominally uniform, a set of computational initial conditions (i.e., spatial profiles of the variables) are calculated for each simulation by satisfying the nominal initial conditions at the domain boundaries and the boundary conditions at R_d . In practice this is achieved by choosing target values for

$$\eta_Y \equiv \left(\frac{dY}{dr} \right)_{r=R_d} \frac{R_d^0}{(1 - \epsilon_r)[Y_e^0 - Y^0(R_d^0)]} \quad \text{and} \quad \eta_T \equiv \left(\frac{dT}{dr} \right)_{r=R_d} \frac{R_d^0}{(1 - \epsilon_r)[T_e^0 - T^0(R_d^0)]} \quad (26)$$

where $\epsilon_r \equiv R_d^0/R_e^0 \ll 1$, and iterate on the values of η_Y , η_T and the dependent variables at the boundary $[Y_1^0(R_d^0)$, $T^0(R_d^0)$ and the rate of oxygen emission from the drop] until convergence is achieved or until a minimal deviation from the targets is obtained.

These simulations were performed on a dual processor 300 MHz personal computer and typical run times were 1 to 2 h.

Results illustrating the R_s^2 variation with t and the corresponding slope of these curves are presented in Figs. 1a and 1b, respectively. As

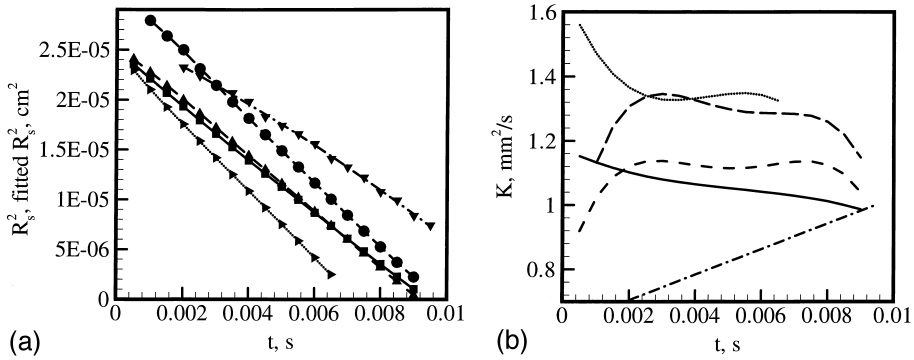


Fig. 1. (1a) Variation of R_s^2 with t for isolated drops. The simulations correspond to the runs listed in Table 1. Symbols correspond to values obtained at the output points, whereas the curves correspond to an n^{th} order, best polynomial fit. 1.5 MPa: simulation output \blacksquare , 4th order polynomial fit (—); 3 MPa: simulation output \blacktriangle , 5th order polynomial fit (---); 6 MPa: simulation output \blacktriangledown , 2nd order polynomial fit (-·-·-); 10 MPa: simulation output \blacktriangleright , 4th order polynomial fit (····); 20 MPa: simulation output \bullet , 5th order polynomial fit (—). (1b) Variation of the slope of the fitted $R_s^2(t)$, K , with time. 1.5 MPa (—); 3 MPa (---); 6 MPa (-·-·-); 10 MPa (····); 20 MPa (—).

explained in the Model section, the value of R_s is chosen to be that of the maximum density gradient location such as to be relevant to optical observations and to the identification of the phase change surface at subcritical pressures. The plotted values of R_s^2 are at discrete intervals that would correspond to several hundred of time steps. Moreover, because it is only the potentially linear part of the curve that is of interest, the initial results pertaining to the heat up time have been removed from the plot, explaining why the curves do not all start at the same ordinate; that is, early time output points which could not be incorporated into a polynomial fit, representing transients due to initial conditions, are not shown. Displayed in Fig. 1a are both the output points values as symbols, and n^{th} order polynomial fits as curves representing the best fit of the output points for each of the runs. As it turns out, best fits were obtained with 4th, 5th, 2nd, 4th, and 5th order Chebychev polynomials, as pressure increases. The fitted curves appear to be almost linear, despite the lack of any assumption that may lead to such behavior. Depicted in Fig. 1b is the value of the slope of all curves displayed in Fig. 1a; for subcritical pressures, this slope is the evaporation constant, K , characterizing the classical d^2 -law. As expected, at 1.5 MPa the value of K is nearly constant, following closely the d^2 -law behavior. However, K is not strictly constant, in agreement with our results [14, 15] for heptane drops in nitrogen showing that

departures from the linear behavior of d^2 with t occur even for pressures slightly in excess of atmospheric. For larger pressures, departures from the linear d^2 behavior are evident, with the largest departure occurring around the O_2 critical point where K cannot be considered constant even for a limited time range. In agreement with the experimental results of Nomura et al. [29] and Sato [41] obtained with heptane drops in nitrogen, K has a nonmonotonic variation with pressure, first increasing, then decreasing around the critical point, and finally increasing again to reach an almost asymptotic behavior. Both Nomura et al. [29] and Sato [41] found this nonmonotonic behavior in examining their data, and Sato [41] found a maximum of the drop lifetime (i.e., a minimum in the value of K) in the vicinity of the critical pressure (supercritical side) of the pure species, similar to the present predictions.

The lack of consistent linear variation of R_s^2 with t raises the question of a possibly different, but nevertheless still simple variation in $R_s^2(t)$ that could be incorporated into rocket combustor design codes to enhance the realism of their predictions. Depicted in Fig. 2 are two such possibilities: lines represent first order Chebychev polynomial fits of R_s^2 which by design yield a constant K , whereas symbols represent second order Chebychev polynomial fits of R_s^2 giving the possibility of a linear $K(t)$ variation. Except for the lower, subcritical pressures, and for the largest pressure of the simulations, the linear

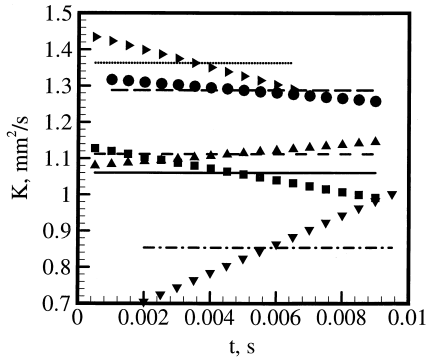


Fig. 2. Fitted values of K . The lines represent first order, and symbols represent second order Chebychev polynomial fits of R_s^2 output points. 1.5 MPa: (—), ■; 3 MPa: (---), ▲; 6 MPa: (-·-·-), ▼; 10 MPa: (····), ►; 20 MPa: (—), ●.

$K(t)$ differs considerably from the value of the constant K . Although the exact variation with pressure of the departure of K from a constant value might change according to the initial temperature of the LOX drop and of H_2 , as well as according to the drop size, it is clear that the d^2 variation is not generally linear for isolated LOX drops in H_2 . Such an assumption might lead to erroneous results and should be reconsidered.

Also important is the observation that, compared with the C_7H_{16}/N_2 behavior described in [14] and [15], here the d^2 -law estimate of the drop lifetime based upon the value of the R_s^2 slope at the end of the heat up period would moderately underestimate the drop lifetime (except at 10 MPa), whereas in our previous isolated drop study [14, 15] it was shown to considerably overestimate the drop lifetime. It is clear that this aspect is species dependent, and caution should be exercised in inferring conclusions from one binary species system to another.

Clusters of Drops

Simulations using the above set of equations were performed for an extensive range of parameters but only a subset is discussed here and is listed in Table 1; the reduced pressure, p_r , listed in the table is calculated with respect of the p_c of O_2 . Similar to the single drop studies, the initial drop and far field temperature were 120 K and 1,000 K, respectively. The initial conditions were calculated in the same manner

TABLE 1

List of Simulations Discussed

Run	p , MPa	p_r	α_{BK}	ϕ^0	Nu_C
d6a	6	1.2	0.2	8	10^3
d10a	10	2.0	0.2	8	10^3
d20a	20	4.0	0.2	8	10^3
d40a	40	8.0	0.2	8	10^3
d10b	10	2.0	0.5	8	10^3
d20b	20	4.0	0.5	8	10^3
d40b	40	8.0	0.5	8	10^3
d20c	20	4.0	0.5	4	10^3
d20d	20	4.0	0.5	12	10^3
d20e	20	4.0	0.2	8	10^4
s20	20	4.0	0.5	8	10^3

Names starting with “d” are for binary size clusters and those starting with “s” for single size. The drop’s initial temperature was 120 K and the far field temperature was 1,000 K in all simulations. The cluster radius was 1.25 cm in all calculations.

as for the single drops, from the nominal initial conditions in the interstitial region. These interstitial region values initially coincide with the specified external far field values: T_e , Y_{1e} , and p_e . From the initial LOX to H_2 mass ratio, ϕ^0 , the initial cluster radius, R_C^0 , the specified initial drop sizes, $R_{d,\alpha}^0$, and the relative (to N) drop number, $R^{si,0}$ as well as the number of drops of each size class was calculated. The present study considers binary sizes of drops and the initial drop size in the monodisperse cluster is calculated by an area and drop number averaging, $(R_d^0)^2 = [(R_{d,1}^0)^2 N_1 + (R_{d,2}^0)^2 N_2]/N$. For all present binary size simulations $R_{d,1}^0 = 4 \times 10^{-3}$ cm, $R_{d,2}^0 = 6 \times 10^{-3}$ cm, and $N_1/N_2 = 20$; therefore, for the monodisperse run $R_d^0 = 4.12 \times 10^{-3}$ cm. Because size Class 1 and the monodisperse drops have essentially the same initial size, comparisons of the fate of these drops during otherwise similar initial conditions simulations should provide the result of including a small number of large drops in the cluster.

Depending on the initial conditions, runs on the dual processor 300 MHz personal computer typically lasted 2 to 3 hs, simulating an extended physical time up to 0.2 s or 0.25 s. Examination of the results showed that all profiles were already well relaxed by 10^{-2} s, and therefore, we will focus the discussion of the results on the time during which a density gradient is easily

identifiable, enabling the ‘optical’ definition of a drop. This definition of the drop does not enter the calculations since the same equations are solved in the entire domain of the sphere of influence including the drop [14, 15, 27]; it is only used for potential comparisons with experiments, or for the purpose of identifying simple time variations.

Effect of the Thermal Diffusion Factor

Magnitude and of Nu_C

Although for C_7H_{16}/N_2 we determined the approximate values of α_{BK} from comparison with data [14, 15], considering that these values are not usually known, we documented in a previous investigation [42] the effect of α_{BK} and α_{IK} in the context of a C_7H_{16}/N_2 shear layer. We determined that at fixed pressure α_{BK} influences the mixing, being directly related to the molar flux, and α_{IK} influences entrainment through its direct relationship to the heat flux cross term thereby influencing the enthalpy, temperature and density profile. Because these conclusions are dependent on the values of the thermodynamic function α_h , a similar study was conducted for LOX/H_2 at 20 MPa; additionally, here we also focus on the effect of the value of α_{BK} at different pressures: 10, 20, and 40 MPa. Simulations are performed for $\alpha_{BK} = 0.2$ and 0.5 (Table 1).

Figure 3 plots are of $\alpha_D \nabla Y_1$ and equivalent terms proportional to ∇T in the drop sphere of influence at 5×10^{-3} s, all being calculated from the numerical solution output of the equations, thus explaining the low level fluctuations due to gradients computed on a grid. The plotted quantities are:

Mass flux and Dufour term

$$\alpha_D \nabla Y_1 \quad (27)$$

Soret term

$$Y_1 Y_2 \alpha_{BK} \frac{\nabla T}{T} \quad (28)$$

Fourier term

$$\left[Y_1 Y_2 \alpha_{BK} + \frac{C_p}{R_u} \frac{Le}{(\alpha_h + \alpha_{BK})} \frac{m_1 m_2}{m^2} \right] \frac{\nabla T}{T} \quad (29)$$

where $Le = \lambda/(\rho C_p D)$. The results of Fig. 3a show that the mass flux and Fourier terms dominate the Soret term, but that this latter is not negligible and becomes progressively more important with increasing pressure as shown in Fig. 3b. Figure 3b intentionally illustrates results at a very high pressure so as to emphasize the increasing influence of the value α_{BK} with p ; however, the actual value of α_{BK} affects mainly the Soret term, in agreement with the results from our previous study [42]. Because the Soret term plays only a moderate role in the range of pressures investigated (10–40 MPa), we conclude that lack of knowledge of its exact value will have only a moderate influence on the quantitative (and certainly none on the qualitative) accuracy of the results. The same findings prevail at fixed time for the larger size class (Fig. 3c and 3d). For both size classes the mass gradient effect is stronger and the Fourier effect is weaker at larger p_e , this being explained by the faster drop temperature profile relaxation. Fourier terms reach maximal magnitude closer to the drop ‘optical’ boundary than Dufour terms, and the former increase whereas the latter diminish with decreasing α_{BK} ; thus the overall variation of the heat flux is not obvious. However, plots of the heat flux (not shown) display a reduced heat flux at the edge of the sphere of influence for smaller α_{BK} , consistent with the higher T^i and smaller ρ^i (not shown), with a consequent increase in R_C and a reduction in the drop number density; the effects are negligible at 10 MPa, but increase with p_e . As for T^i , Y^i , and ρ^i at fixed p_e , they are not affected by α_{BK} because this is a region of uniformity; in fact the magnitude of T^i , Y^i , and ρ^i is dominated by the value of Nu_C (not shown).

The influence of Nu_C on a cluster of drops has been documented before [34] and it has been shown that as it increases the cluster expands more rapidly due to increased heat transfer from the far field; however, no conclusions were presented regarding dependence of the d^2 variation upon the value of Nu_C . Figure 3e documents the influence of the Nu magnitude on the present predictions and shows consistently the same increase in the magnitude of fluxes and the enlargement of the sphere of influence as in [34]. Figure 4a illustrates the

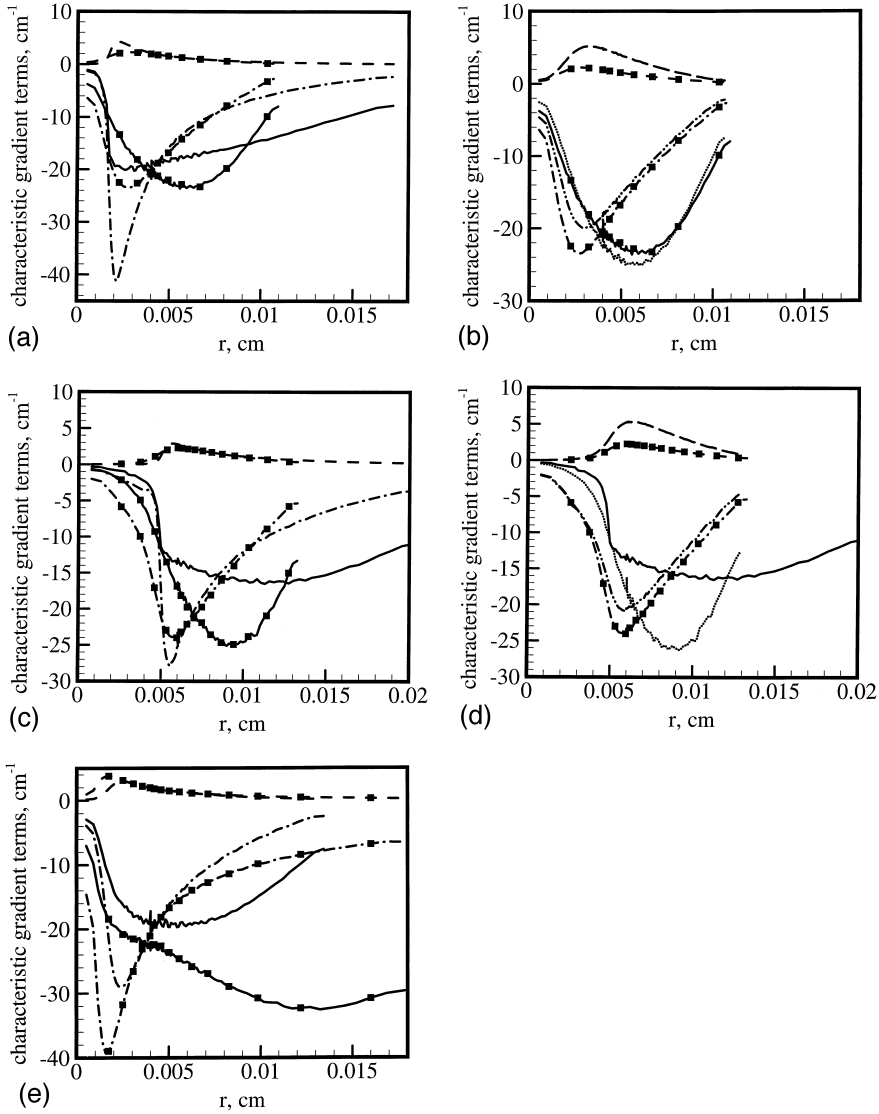


Fig. 3. Characteristic gradient terms for the mass, Soret and Fourier contributions (the mass term is the Dufour term in the heat flux) at $t = 5 \times 10^{-3}$ s. (3a): gradients for fixed α_{BK} as a function of p for $R_{d,1}$; (3b): gradients at fixed p as a function of α_{BK} for $R_{d,1}$; (3c): gradients for fixed α_{BK} as a function of p for $R_{d,2}$; (3d): gradients at fixed p as a function of α_{BK} for $R_{d,1}$. For 3a–3d: mass gradient term 10 MPa, $\alpha_{BK} = 0.2$ (—); 40 MPa, $\alpha_{BK} = 0.2$ (—■—); 40 MPa, $\alpha_{BK} = 0.5$ (····); Soret term 10 MPa, $\alpha_{BK} = 0.2$ (---); 40 MPa, $\alpha_{BK} = 0.2$ (---■---); 40 MPa, $\alpha_{BK} = 0.5$ (—); Fourier term 10 MPa, $\alpha_{BK} = 0.2$ (---); 40 MPa, $\alpha_{BK} = 0.2$ (---■---); 40 MPa, $\alpha_{BK} = 0.5$ (---·---). (3e) 20 MPa results: mass gradient term $Nu = 10^3$ (—), $Nu = 10^4$ (—■—); Soret term $Nu = 10^3$ (---), $Nu = 10^4$ (---■---); Fourier term $Nu = 10^3$ (---·---), $Nu = 10^4$ (---·■---).

optical drop area, A_s , calculated using the location of the maximum density gradient and shows that the d^2 -law is not followed as the curves have definite positive curvatures. However, with increasing Nu_C the drops diminish faster, and d^2 has a more nearly linear variation. It should be recalled that the d^2 -law results from a quasi-

steady solution and portrays physics which is different from that of supercritical behavior, and therefore, there is no reason to expect it to hold in this regime.

Illustrated in Fig. 4b is the corresponding variation as a function of p_e of the difference, A^* , between A_s and a linear function of t [i.e.,

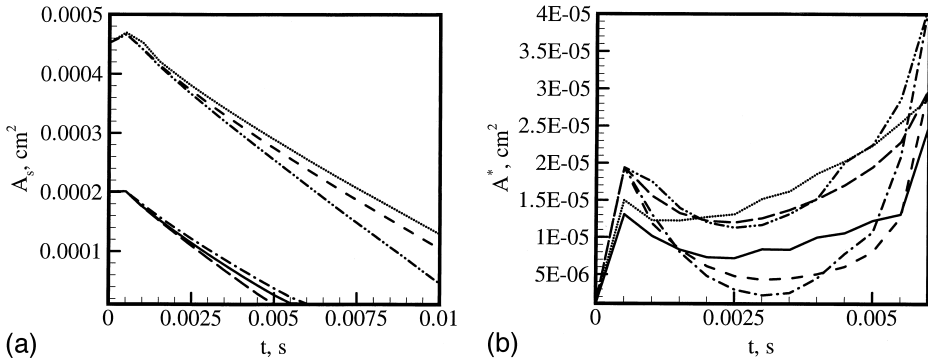


Fig. 4. (a) Time variation of the drop area for Runs d20a [$R_{d,1}$ (—); $R_{d,2}$ (---)]; d20b [$R_{d,1}$ (---); $R_{d,2}$ (····)]; d20e [$R_{d,1}$ (—); $R_{d,2}$ (---)]; (b) Time variation of the difference between the drop area and the linear function of t [$2 \times 10^{-4}(1 - t/5.5 \times 10^{-3})$] for Runs d10a (—); d20a (---); d40a (---); d10b (····); d20b (—); d40b (---)] for $R_{d,1}$.

$2 \times 10^{-4}(1 - t/5.5 \times 10^{-3})$] whose ordinate at $t = 0$ approximately corresponds to the initial value of the drop area and whose slope is equal to the average slope of the A_s curves. Therefore, this plot emphasizes both the difference between the results for different values of p_e and the possible departures from a linear variation with t . Similar to previous results with C_7H_{16}/N_2 [14, 15], and to the isolated LOX/H_2 findings above, even after the initial heat up time during which the drop may sometimes grow in size, the d^2 -law is not followed, and this conclusion is independent of the α_{BK} magnitude.

The general conclusions are that ∇Y terms increase and ∇T terms decrease as either p_e or α_{BK} increase, with the ∇T terms being larger for the smaller drops at the smallest p_e . However, all gradient terms increase with Nu_C . The resulting A_s relaxes faster with either increasing p_e or Nu_C , or with decreasing α_{BK} .

Aspects of Polydispersity

Smaller Versus Larger Drops Behavior. Illustrated in Fig. 5 is A_s for 6, 10, 20 and 40 MPa with $\alpha_{BK} = 0.2$. Clearly, the drop size decreases faster with increasing pressure, however there seems to be a much greater differentiation between the situation at 6 MPa, which is near the oxygen critical point and the other pressures which are far from the critical point. This finding supports the hydrocarbon/ N_2 observations of Nomura et al. [29] and of Sato [41] that the drop lifetime decreases with pressure in the supercritical regime. Moreover, we find that the lifetime of the small drops is considerably

shorter, consistent with the quicker temperature rise in the sphere of influence, and consequent higher relaxation rate of the density in the same region (not shown); however, the rate of disappearance of the two drop sizes is similar. It should be realized that the physics of drop disappearance is here quite different from that in the subcritical regime where evaporation and convective-diffusive processes were governing; in contrast, in the supercritical regime the governing phenomenon is only that of diffusion [14, 15], and the rate of oxygen emitted from the drop is null. The local departures from smooth behavior occurring at 6 MPa for the larger drops are attributable to the sparse nature of the output points and to the enlarged scale of the graph, as a smooth variation appears when plotted over their entire lifetime.

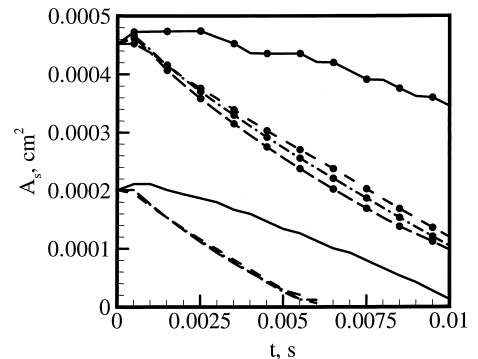


Fig. 5. Time variation of the drop area corresponding to Runs d6a [$R_{d,1}$ (—); $R_{d,2}$ (—●—)]; d10a [$R_{d,1}$ (---); $R_{d,2}$ (---●---)]; d20a [$R_{d,1}$ (---); $R_{d,2}$ (---●---)]; d40a [$R_{d,1}$ (—); $R_{d,2}$ (—●—)].

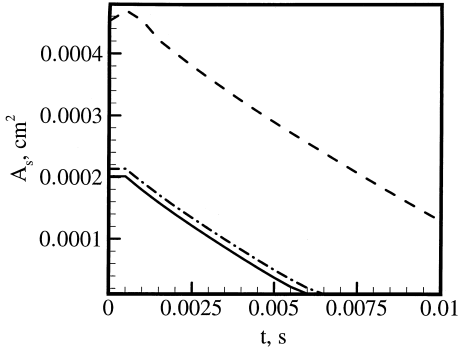


Fig. 6. Time variation of the drop area corresponding to Runs d20b [$R_{d,1}$ (—); $R_{d,2}$ (---)] and s20 (— · —).

Monodisperse Versus Polydisperse Clusters. To examine the effect of polydispersity under supercritical conditions we compared 20 MPa results from a monodisperse cluster of drops of 4.12×10^{-3} cm initial radius with those from the two size classes in the binary size cluster. Depicted in Fig. 6 is A_s for these three drop sizes. In a binary size cluster under subcritical conditions, the smaller size class would disappear faster than similar size drops in a monodisperse cluster because in the former situation the total mass in the smaller drops is lower with consequent reduced latent heat requirement. Under supercritical conditions we also find that the smaller drops in a binary size cluster with a large N_1/N_2 disappear faster than similar size drops in a monodisperse cluster, although it is no longer due to evaporative processes; instead, due to their smaller size these drops heat up faster inducing a correspondingly faster relaxation of the density. However, the larger size drops persist well after the smaller drops disappear, and therefore, when approximating a polydisperse cluster of drops by a monodisperse one, although reproducing well the cluster growth and the interstitial variables values (not shown), one underestimates the cluster lifetime (time when the density gradient is totally relaxed).

Effect of the LOX/ H_2 Initial Mass Ratio. To explore the influence of the LOX/ H_2 initial mass ratio, ϕ^0 , we conducted simulations with $\phi^0 = 4, 8$, and 12 (initial values of R^{si} are 1.53×10^{-2} cm, 1.19×10^{-2} cm and 1.03×10^{-2} cm, respectively) at 20 MPa, and the resulting A_s is displayed in Fig. 7. Consistent with mass diffu-

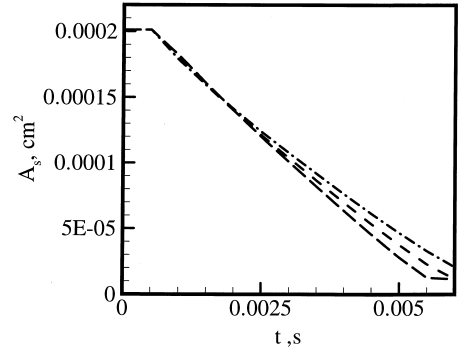


Fig. 7. Time variation of the drop area corresponding to $R_{d,1}$ in Runs d20c (—); d20b (---); and d20d (— · —).

sional processes in the presence of heat transfer, the drop lifetime is larger with increasing ϕ^0 ; however, the new result is the increased departure from the d^2 -law behavior with increasing ϕ^0 . Indeed, when fluid is heated it will expand and the result will be a reduction in the magnitude of gradients as well as in that of fluxes. The extended drop lifetime is attributed to the decreased magnitude of the heat and mass fluxes (not shown). The increased departure from a linear d^2 variation with increased lifetime that occurs for larger ϕ^0 is consistent with that of the Nu_C effect in that with decreasing drop lifetime d^2 assumes a variation close to linear.

Departures From the Ideal Mixture and Perfect Gas Conditions. Previous studies of the C_7H_{16}/N_2 system [15, 42] have identified considerable departures from the ideal mixture ($\alpha_D = 1$), perfect gas ($Z = pv/(R_u T) = 1$) situation. Plots of α_D displayed in Fig. 8a indeed portray mixtures that are initially highly non-ideal, tending, as expected, towards ideality as the drops disappear. Radial profiles, such as those in Fig. 8a, always display a minimum at the drop ‘optical’ boundary showing that it is there that the mixture is closer to the critical point ($\alpha_D = 0$); values as low as $\alpha_D = 0.2$ are encountered for 6 MPa. Smaller drops have smaller α_D ’s, indicating that they may be more prone to reaching critical conditions at the boundary. Evaluations of Z shown in Fig. 8b illustrate the difference between the state of the drop compared to a liquid: $Z \sim 0.2$ at 6 MPa on the LOX side of the boundary, indicating that the drop is neither a liquid ($Z \ll 1$) nor an ideal gas ($Z = 1$); however, the state of the

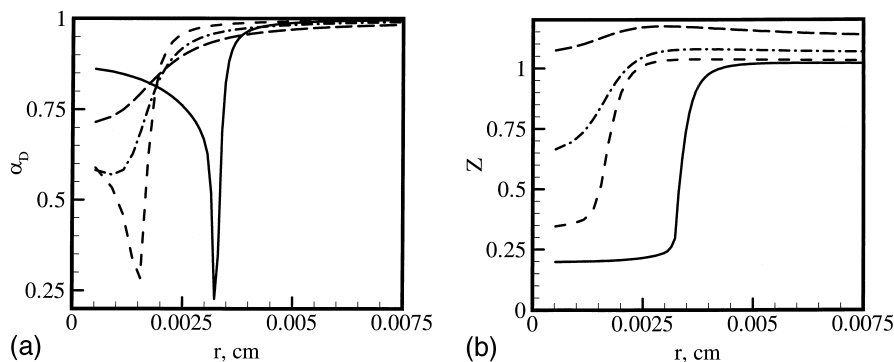


Fig. 8. Radial variation at $t = 5 \times 10^{-3}$ s of the mass diffusion factor (8a) and compression factor (8b) in the drop sphere of influence for size Class 1 for 6 MPa (—), 10 MPa (---), 20 MPa (-·-·-), and 40 MPa (— —) corresponding to Runs d6a–d40a.

drop's surrounding at 6 MPa is essentially that of an ideal gas. With increasing pressure Z increases as well, reaching at 40 MPa values in excess of 1 in both sides of the drop boundary, the value in the initially H_2 side being always larger.

CONCLUSIONS

A validated model for isolated fluid drops has been exercised for isolated LOX drops in H_2 at subcritical and supercritical pressures in order to elucidate the d^2 variation as a function of pressure. The formulation includes accurate equations of state, and accurate definitions and values of the transport properties. Validation of the isolated drop model for C_7H_{16} drops in N_2 required using part of the data for evaluating the thermal diffusion factor for C_7H_{16} drops in N_2 and the experimental validation of the present results would also depend upon finding the correct values of the O_2/H_2 thermal diffusion factor. Because a similar data set was not available here, we used as a guideline the low pressure thermal diffusion factor value for O_2 in H_2 and further examined the influence of its value in the context of drop clusters.

The isolated drop results show that while in the low pressure subcritical regime the d^2 variation is nearly linear, with increasing pressure there are considerable departures from linearity. Constant and linear fits of the $d^2(t)$ slope, which at subcritical pressures is the evaporation constant, showed that the assumption of it being

constant may be in substantial error. The linear fits exhibited both increasing and decreasing trends, indicating that $d^2(t)$ may have either positive or negative curvatures, according to the pressure. Since for isolated C_7H_{16} drops in N_2 we found consistently a negative curvature, we conclude that the curvature is species dependent.

Conservation equations describing a polydisperse fluid-drop cluster behavior under quiescent far field conditions have been derived and exercised for LOX drops in H_2 at supercritical pressures. Comparisons of characteristic gradient terms for two values of the thermal diffusion factor showed, consistently with other previous results, that the thermal diffusion factor influences mostly the Soret term. This latter, although not negligible, was shown to be dominated both by the mass gradient term (Fick's or Dufour) and by the Fourier term. An increase by a factor of 2.5 in the thermal diffusion factor was shown to yield only modest changes in the Dufour and Soret terms. In fact, the interstitial thermodynamic quantities are insensitive to the value of the thermal diffusion factor up to 40 MPa where a modest sensitivity is apparent. What controls the magnitude of the interstitial quantities is the value of the cluster Nusselt number; however, an order of magnitude increase in the Nusselt number reduces the drop disappearance time only by a small fraction, thus reflecting the diffusive nature (large characteristic times) of the situation.

Under all conditions of this polydisperse clus-

ter study, encompassing 6 to 40 MPa ($p_r = 1.2 - 8$) and a LOX/H_2 mass ratio of 4 to 12, the variation of d^2 is not linear and the curves consistently exhibit a positive curvature. Comparing with the isolated drop results, this indicates that the d^2 variation is not only species-, but also configuration-dependent.

Comparisons of results from a binary size cluster of drops containing a much larger proportion of small drops with those from a monodisperse cluster where the drop size is the area based average of the two size classes, shows that although the interstitial quantities may be well predicted by a monodisperse approximation, the lifetime of the cluster is significantly underestimated.

All present results display the departures from the perfect gas law and mixture ideality epitomizing the supercritical conditions. For example, the compression factor exhibits values $O(10^{-1})$ inside the drop which significantly depart from the $O(10^{-3})$ for liquids and $O(1)$ for perfect gases, whereas the mass diffusion factor may decrease as low as 0.2, considerably deviating from the ideal mixture unity value.

This research was conducted at the Jet Propulsion Laboratory under sponsorship from the National Aeronautics and Space Administration, the George W. Marshall Space Flight Center with Klaus W. Gross as technical contract monitor. His continuing interest and support are greatly appreciated.

REFERENCES

- Givler, S. D., and Abraham, J., *Prog. Energy Combust. Sci.* 22:1–28 (1996).
- Bellan, J., *Prog. Energy Combust. Sci.*, 26:329–366 (2000).
- Chesneau, X., Chauveau, C., and Gökalp, I., Experiments on high pressure vaporization of liquid oxygen droplets, AIAA 94-0688, 32nd Aerospace Sciences Meeting, Reno, NV., 1994.
- Krülle, G., and Mayer, W., *Proc. of ICLASS 1994*, Rouen, France.
- Mayer, W., and Tamura, H., *J Propulsion and Power*, 12(6):1137–1147 (1996).
- Mayer, W., Schik, A., Schweitzer, C., and Schäffler, M., Injection and mixing processes in high pressure LOX/GH_2 rocket combustors, AIAA 96-2620, AIAA/SAE/ASME/ASEE 32nd Joint Propulsion Conference, 1996.
- Mayer, W., Ivancic, B., Schik, A., and Hornung, U., Propellant atomization in LOX/GH_2 rocket combustors, AIAA 98-3685, 34th AIAA/ASME/SAE/ASEE Propulsion Conference, 1998.
- Chehroudi, B., Talley, D., and Coy, E., Initial growth rate and visual characteristics of a round jet into a sub-to supercritical environment of relevance to rocket, gas turbine, and diesel engines, AIAA 99-0206, 37th Aerospace Sciences Meeting, 1999.
- Chehroudi, B., Talley, D., and Coy, E., AIAA 99-2489, Fractal geometry and growth rate changes of cryogenic jets near the critical point, 35th AIAA/ASME/SAE/ASEE Joint Propulsion Conference, 1999.
- Oschwald, M., Schik, A., Klar, M., and Mayer, W., Investigation of coaxial LN_2/GH_2 -injection at supercritical pressure by spontaneous Raman scattering, AIAA 99-2887, 35th AIAA/ASME/SAE/ASEE Joint Propulsion Conference, 1999.
- Ivancic, B., Mayer, W., Krülle, G., and Brüggemann, D. Experimental and numerical investigation of time and length scales in LOX/GH_2 -rocket combustors, AIAA 99-2211, 35th AIAA/ASME/SAE/ASEE Joint Propulsion Conference, Los Angeles, CA, 1999.
- Snyder, R., Herding, G., Rolon, J. C., and Candel, S., *Combust. Sci. and Tech.*, 124:331–370 (1997).
- Harstad, K., and Bellan, J., *Int. J. of Multiphase Flow*, 23(5):899–925 (1997).
- Harstad, K., and Bellan, J., A validated all-pressure fluid drop model for binary mixtures: heptane in nitrogen, AIAA 99-2206, Joint AIAA/ASME/SAE Propulsion Meeting, 1999.
- Harstad, K., and Bellan, J., *Int. J. of Multiphase Flow*, 26(10):1675–1706 (2000).
- Rosner, D. E., *AIAA J.*, 5(1):163–166 (1967).
- Rosner, D. E., and Chang, W. S., *Comb. Sci. Tech.*, 7:145–158 (1973).
- Umemura, A., *Proc. of the Combustion Institute*, 21: 463–471 (1986).
- Jia, H., and Gogos, G., *J. Thermophysics and Heat Transfer*, 6(4):738–745 (1992).
- Jia, H., and Gogos, G., *Int. J. Heat Mass Transfer*, 36(18):4419–4431 (1993).
- Delplanque, J-P., and Sirignano, W. A., Stability influence of transcritical LOX droplet vaporization in an idealized rocket combustor, AIAA 93-0231, 31st Aerospace Sciences Meeting, Reno, NV, 1993.
- Yang, V., Lin, N., and Shuen, J-S., *Combust. Sci. and Tech.*, 97:247–270 (1994).
- Hsiao, G. C., Yang V., and Shuen, J. S., Supercritical vaporization and dynamics of liquid oxygen (LOX) droplet in hydrogen stream, AIAA 95-0383, 33rd Aerospace Sciences Meeting, Reno, NV, 1995.
- Daou, J., Haldenwang, P., and Nicoli, C., *Combust. Flame*, 101:153–169 (1995).
- Umemura, A., and Shimada, Y., *Proc. of the Combustion Institute*, 26:1621–1628 (1996).
- Umemura, A., and Shimada, Y., *Proc. of the Combustion Institute*, 27:2659–2665 (1998).
- Harstad, K., and Bellan, J., *Int. J. Heat Mass Transfer*, 41:3537–3550 (1998).
- Harstad, K., and Bellan, J., *Int. J. Heat Mass Transfer*, 42:961–970 (1999).

29. Nomura, H., Ujiie, Y., Rath, H. J., Sato, J., and Kono, M., *Proc. of the Combustion Institute*, 26:1267–1273 (1996).
30. Morin, C., Vaporization et oxidation à haute température et haute pression de gouttes de combustible liquides. Application aux n-alcanes et esters méthyliques d'huiles végétales, Ph.D. thesis, Centre National de la Recherche Scientifique, Orléans, France, 1999.
31. Jiang, T. L., and Chiang, W-T., *Comb. Flame*, 97:17–34 (1994).
32. Jiang, T. L., and Chiang, W-T., *Combust. Flame*, 97:355–362 (1994).
33. Jiang, T. L., and Chiang, W-T., *Int. J. Heat Mass Transfer*, 39(5):1023–1031 (1996).
34. Harstad, K., and Bellan, J., *Int. J. Heat Mass Transfer*, 41:3551–3558 (1998).
35. Keizer, J., *Statistical Thermodynamics of Nonequilibrium Processes*, Springer-Verlag, New York, 1987, p. 42–91, 256–269.
36. de Groot, S. R., and Mazur, P., *Nonequilibrium Thermodynamics*, North-Holland, Amsterdam, 1984 p. 30–42, 235–284.
37. Chapman, S., and Cowling, T. G., *The Mathematical Theory of Nonuniform Gases*, Cambridge University Press, Cambridge, 3rd edition, 1970, p. 278.
38. Harstad, K., Miller, R. S., and Bellan, J., *A.I.Ch.E. J.*, 43(6):1605–1610 (1997).
39. Sarman, S., and Evans, D. J., *Phys. Rev.*, A45(4):2370–2379 (1992).
40. Reid, R. C., Prausnitz, J. M., and Polling, B. E., *The Properties of Gases and Liquids*, 4th Edition, McGraw-Hill Book Company, 1987, p. 491–576.
41. Sato, J., Studies on droplet evaporation and combustion in high pressures, AIAA 93-0813 31st Aerospace Sciences Meeting, 1993.
42. Miller, R. S., Harstad, K. G., and Bellan, J., accepted to *J. Fluid Mech.*, (2000).

Received 10 February 2000; revised 23 August 2000; accepted 6 September 2000